Quantitative Microstructural Imaging by Scanning Laue X-Ray Micro- and Nanodiffraction

Xian Chen[1], Catherine Dejoie[2], Tengfei Jiang[3], Ching-Shun Ku[4] and Nobumichi Tamura[5]*

1 Dept. of Mechanical and Aerospace Engineering, Hong Kong University of Science and Technology, Hong-Kong
2 Lab. of Crystallography, Department of Materials, ETH-Zurich, Switzerland
3 Dept. of Materials Science and Engineering and Advanced Materials Processing Analysis Center, University of Central Florida, Orlando, Florida, US
4 National Synchrotron Radiation Research Center, Hsinchu, Taiwan
5 Advanced Light Source, Lawrence Berkeley National Lab., Berkeley, California, US

*Corresponding author: ntamura@lbl.gov

Local crystal structure, crystal orientation and crystal deformation can all be probed by Laue diffraction using a submicron x-ray beam. This technique, employed at a synchrotron facility is particularly suitable for fast mapping mechanical and microstructural properties of inhomogeneous multi-phase polycrystalline samples as well as imperfect epitaxial films or crystals. As synchrotron Laue X-ray microdiffraction is entering its 20 years of existence and new synchrotron nanoprobe facilities are being built and commissioned around the world, we take the opportunity to give an overview of its current capabilities and latest technical developments. Fast data collection provided by state-of-the-art area detectors and fully automated pattern indexing algorithms optimized for speed make it possible to map large portions of a sample by fine step size and get quantitative images of its microstructure in near real time. Finally, we extrapolate on how the technique will evolve in the near future and its potential emerging application at a free electron laser facility.

Keywords: x-ray diffraction, crystallographic structure, phase transformation

1. Introduction:

Since its discovery in 1912 by Max von Laue, Paul Knipping and Walter Friedrich 1, the now more than a century old technique of x-ray diffraction has become the inescapable tool of choice for probing atomic arrangements in crystalline materials. The formulation of Bragg's law by William Lawrence Bragg and William Henry Bragg in 1913 2, which elegantly explains the formation on photographic plates of discrete sets of reflections, emanating from the x-ray

illuminated crystal, led to the possibility of solving the atomic structure of crystalline compounds and the invention of x-ray crystallography. X-ray diffraction is today used under many forms to characterize materials, including single crystal x-ray diffraction 3, x-ray powder diffraction 4 and grazing incidence diffraction 5. It is worth noting that all the techniques cited above are using a monochromatized incident x-ray beam as the knowledge of the x-ray wavelength is necessary to obtain the inter-atomic spacing.

Polychromatic x-ray diffraction, better known as white beam Laue diffraction, although being the first to be achieved, turned out to be more difficult to interpret and was long solely used to orient crystals before their mounting on a diffractometer for monochromatic x-ray study. Laue x-ray diffraction went through a revival in the 1990s along two different directions. First, it was seen as a viable alternative for solving large unit cell crystal structure for time-resolved studies. While conventional crystallography requires the collection of hundreds of diffraction patterns while the crystal is rotated to get a usable set of reflections, the same set can be obtained in a single shot with Laue diffraction as the Bragg condition is simultaneously satisfied for a range of wavelengths 6 7. With a way of determining the wavelength of each reflection or “calibrating” the size of the crystal unit cell, Laue diffraction is successfully used to solve the structure of ephemeral macromolecular configurations 8 9. Second, it was realized that the fast recording of Laue patterns can be used for mapping crystal orientation 10 and strain 11 in materials. This technique is called x-ray Laue microdiffraction or microLaue diffraction when the x-ray beam size is in the order of 1 μm.

A very small beam is useful for a range of common materials science problems. These include identifying minute amounts of materials in heterogeneous matrices 12, mapping deformation and phase transformation around a crack tip 13, or following plastic deformation in small devices such as a metal interconnect line during electromigration 14. X-ray microdiffraction is generally employed in complement to other spatially resolving and imaging techniques, as it offers information that is not easily obtainable from other characterization tools. Electron microscopy achieves high spatial resolution but requires the sample to be in vacuum and necessitates careful sample preparation 15. None of these restrictions apply to x-ray microdiffraction, as hard x-ray is highly penetrating (from a few microns to hundreds of microns depending on the material and x-

ray energy range) and samples can in principle be measured “as is” without any alteration due to sample preparation. X-rays can probe buried surfaces, such as metal interconnects under a thick layer of dielectric 14 in a variety of sample environments

In this review, we will first present the instrumental settings including apparatus and equipment for Laue x-ray microdiffraction experiments. In the next section, we will show two fields of applications of the technique for structural characterization. Finally, we will present current and expected future developments of the technique.

2. Synchrotron X-Ray Laue Microdiffraction

2.1 Instrumental setup

An x-ray microdiffraction experiment is performed on a dedicated instrument at a synchrotron radiation facility (a beamline end station). Small x-ray beams are generated by efficient brightness-preserving x-ray focusing optics, for which many different types have been developed over the years. The most popular ones are Fresnel zone plates 16 17 18 19, compound refractive lenses (CRL) 20 21 22 and Kirkpatrick-Baez (KB) mirrors 23. Diffractive optics, such as zone plates, and refractive optics, such as CRLs, have chromatic aberration, which made them unsuitable for focusing polychromatic radiation. The optics of choice for white beam applications are therefore achromatic reflective optics, such as KB mirrors. Below a certain critical grazing angle, x-rays are totally reflected by a smooth, reflective surface. If the surface is bent to an elliptical shape, the reflected x-rays converge to a focal point. KB mirrors employ two orthogonal ultra-smooth surfaces coated with a reflective metal layer, to focus the beam both horizontally and vertically, and can achieve spot size well below 100 nm 24 25. A recent development are the nested (or Montel) mirrors where the two mirrors, instead of being separate as in the KB configuration, are combined, resulting in a more compact design 26.

However, even highly efficient optics such as KB mirrors, have a very limited acceptance in the order of a few hundred microns. This is why micron to submicron sized x-ray beams are only achieved at synchrotron radiation facilities, where the x-ray beam is both intense and highly collimated. The very low divergence of the synchrotron x-ray beam, together with a small angular source size, makes it possible to achieve high demagnification. Since synchrotron x-rays are orders

of magnitude brighter than those generated at laboratory sources, photon flux can be "traded" for spot size. Another advantage of synchrotron is its energy tunability, which permits spectroscopic applications. X-ray microdiffraction instruments are often combined with microspectroscopic techniques.

Laue x-ray microdiffraction is best performed with an x-ray synchrotron source providing a continuous spectrum, such as bending magnets and wigglers. There are several dedicated x-ray microdiffraction facilities around the world but few that have Laue microdiffraction capabilities: the Advanced Photon Source undulator beamline ID-34 is historically the oldest of this kind still in operation 27. The superconducting magnet beamline 12.3.2 at the Advanced Light Source 28 was moved in 2008 from an older station on beamline 7.3.3 29. The European Synchrotron Radiation facility (ESRF) in Grenoble, France has a Laue microdiffraction setup on BM32 30, and so has the Pohang Light Source (PLS) on beamline 1B2 31 and the Canadian Light Source (CLS) on the VESPERS beamline 32. Laue x-ray microdiffraction is also performed occasionally at the Swiss Light Source (SLS) on the microXAS beamline 33 and the Diamond B16 beamline 34. In construction, commissioning or planning stage, are the Taiwan Photon Source (TPS) nanodiffraction beamline 21A, the Laue microdiffraction projects at the Shanghai Synchrotron Research Facility (SSRF), and the Australian Synchrotron (AS). We described two of these beamlines the ALS beamline 12.3.2., and the new nanodiffraction beamline at TPS, in more details below.

Figure 1 shows the outline of the 12.3.2 x-ray microdiffraction beamline at the Advanced Light Source 28 35. The x-ray source for this beamline is a superconducting magnet, providing a continuous energy spectrum with a critical energy around 12 keV. The first optical element encountered by the x-ray beam is a toroidal mirror, which refocuses the beam at the entrance of the experimental hutch. A pair of roll slits makes it possible to adjust the source size and thus to vary the x-ray spot size on the sample. A four-bounce monochromator, made of two identical silicon 111 channel cuts can be inserted to obtain a monochromatic instead of a polychromatic beam. The four bounce design ensures that the polychromatic and monochromatic beams follow the same path to the focusing optics and sample, allowing the same spot on the sample be interrogated by both types of radiations. Final x-ray focusing is provided by a pair of elliptically

bent KB mirrors 36, giving a routine spot size on sample of 1 μm in both the horizontal and vertical directions.

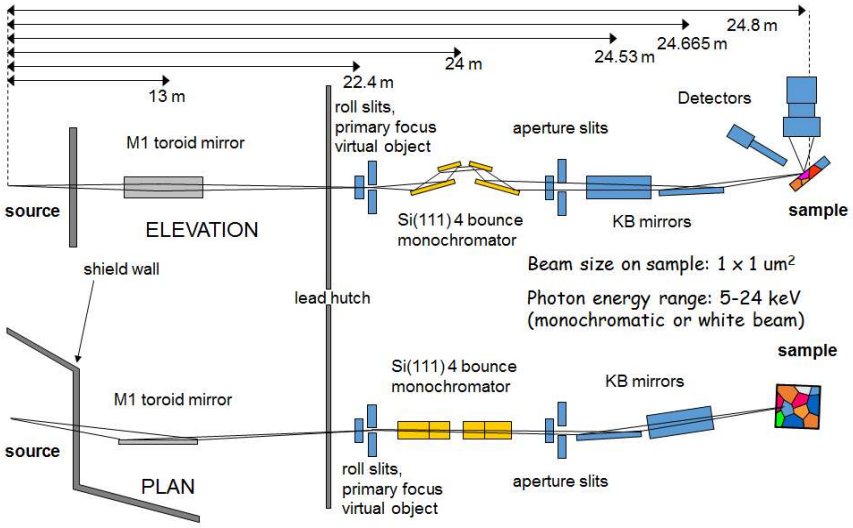

Figure 1. Outline of the x-ray microdiffraction (BL 12.3.2) beamline at the Advanced Light Source (Adapted from Kunz et al., 2009 28)

The sample is mounted on a high precision XYZ stage, sitting on a χ cradle, allowing high flexibility in the sample positioning and navigation, with respect to beam. X-ray detectors consist of a DECTRIS Pilatus 1 M detector to collect diffraction patterns and a VORTEX silicon-drift detector (SDD) to collect x-ray fluorescence (XRF) signal.

The TPS nanodiffraction beamline 21A follows a similar design but offers a wider range of sample-probing capabilities 37. Figure 2 shows a schematic of the future FOcus x-Ray for MicrO-Structure Analysis (FORMOSA) end station. FORMOSA provides an all-in-one solution including Differential Aperture X-Ray Microscopy (DAXM) (see section 2-2), XRF, X-ray excited optical luminescence (XEOL)/Raman/Photoluminescence, nanoscale x-ray absorption spectroscopy (nXAS), scanning probe microscopy based I-V and indenter to perform in-situ and in-operando measurements for structural, elemental, optical, electrical and mechanical properties. Built-in scanning electron microscopy (SEM) and secondary electron detector (SED) provides real-time images for sample navigation and positioning. Nominal expected spot size on the sample is 100 nm provided by fixed shaped KB mirrors from JTEC corporation.

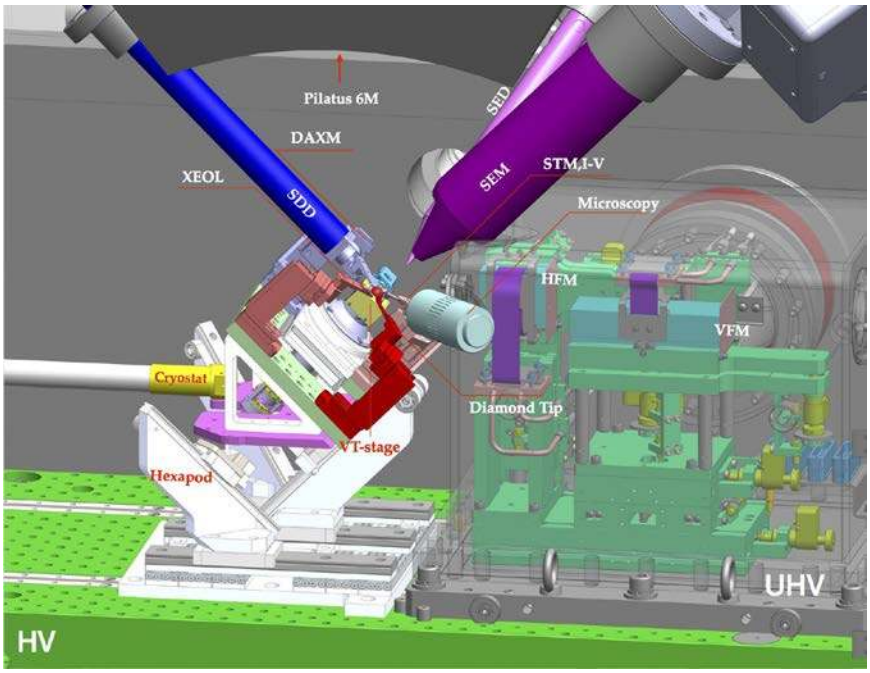

Figure 2. An inside view of the FORMOSA (FOcus x-Ray for Micro-Structure Analysis) end-station at the TPS.

2.2 Data collection

Back-reflection Laue is extensively used to determine single crystal orientation 38. Spatial resolution provided by x-ray focusing optics adds new capabilities to this old technique. Samples can be raster scanned under the focused x-ray beam, while Laue patterns are taken at each step. Similar to the indexing of arrays of Kikuchi patterns in EBSD, the indexing of the arrays of Laue patterns provides an orientation map of the sample 10 39 40.

The use of a large area detector with one or more megapixels resolution also brings the possibility to measure subtle changes in the diffraction peak positions and shapes. From the relative shifts of the Laue spots from their "ideal" positions, as expected from an unstrained crystal, the deformation of the unit cell can be calculated and the full deviatoric (or distortional) strain tensor derived 11. Scanning x-ray Laue microdiffraction can therefore provide the distribution of the elastic strains in the material. The shape of the Laue spots also contains information about crystal mosaicity as well as plastic deformation. Streaking of reflections along certain directions are generated by geometrically necessary dislocations 41 while splitting of these same reflections reveal the

existence of small angle grain boundaries. Laue x-ray microdiffraction is therefore ideally suited for the spatially resolved study of materials mechanical properties.

A further development of scanning Laue x-ray microdiffraction is the addition of depth resolution, which transforms the instrument from a 2D mapping tool into a 3D reconstruction tool. DAXM 42 43 (Figure 3) uses a scanning metal wire as a knife-edge to ray-trace back the origin of the diffracted x-ray beams inside the material. A Laue pattern collected at a single location is a composite of all Laue diffractions occurring along the path of the incident x-ray beam, which can penetrate several tens of microns into the sample. DAXM deconvolutes the Laue patterns from different depths inside the sample, giving access to the third dimension. The analysis of a DAXM scan produces a volumetric map of crystal orientation and elastic strain in the sample 44.

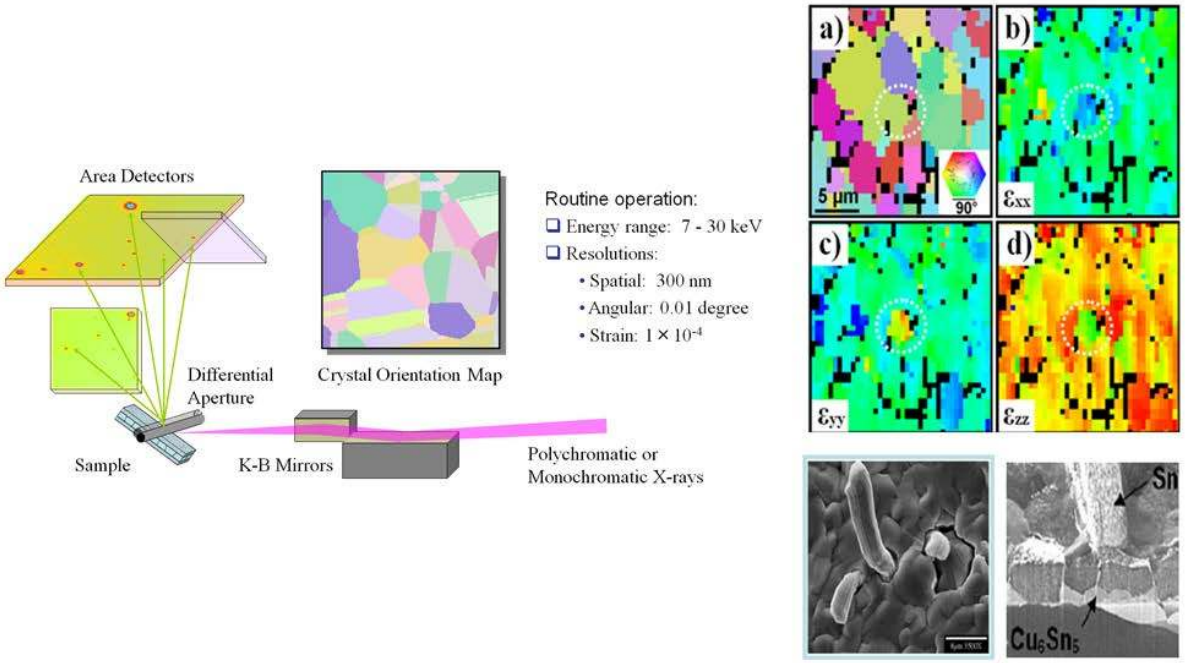

Figure 3. Principle of the Differential Aperture X-Ray Microscopy (DAXM) technique and results of a DAXM scan under a tin whisker. a) orientation map, b),c) d) strain maps along the in plane x and y direction and the out-of-plane z direction (Courtesy of Wenjun Liu, from 43).

3. Applications for Laue x-ray microdiffraction

With its high sensitivity to crystal orientation, elastic strain and plastic deformation, Laue x-ray microdiffraction has been widely used to study the microstructure and mechanical properties of

very small devices, such as microelectronic components. It can also be used to completely characterize structural changes during a phase transformation *in-situ*. This section gives some recent applications of the technique in these two fields.

3.1. In-situ investigation of martensitic transformation by Laue X-ray Microdiffraction.

Martensitic transformation is a solid-solid phase transformation occurring reversibly between two crystal structures with different symmetries. Materials undergoing such transformations exhibit shape memory effects and superelasticity, widely exploited for medical devices 45, microelectronic sensors 46 47 and energy conversion devices 48 49 50 51. A major problem with these materials is the lack of phase reversibility upon cyclic loading. Two recent discoveries in ZnAuCu and NiTiCu shape memory alloys 52 53 have revealed a strong microstructure – property correlation, i.e. when the lattice parameters of the material satisfy a set of compatibility conditions 54, both thermal and mechanical behaviors become completely reversible even after tens of millions of transformation cycles, and lead to the formation of rich microstructural morphologies. Using a thermal stage to quasi-statically heat/cool the sample through its phase transition temperature while continuously collecting Laue patterns, we have tracked the phase transformation pathway from austenite to martensite for the shape memory alloy $Zn_{45}Au_{30}Cu_{25}$ 55, by monitoring the spatial variations of specific (hkl) planes as well as the overall change in lattice orientation (Figure 4).

The material undergoes martensitic transformation from cubic ($a_0 = 6.1606$Å) to monoclinic ($a = 4.458$ Å, $b = 5.768$ Å, $c = 40.698$ Å and $\beta = 86.8°$) at -40°C 52. When the sample is in the pure austenitic phase at -10℃, a strong diffraction peak by the cubic (206) plane is visible in Figure 4(a). Upon cooling through the transition temperature, this diffraction spot splits into three weaker reflections while several other reflections appear. It indicates that the cubic symmetry is breaking down and that the original interplanar distance of (206) is changing. Using the austenite structure to index the Laue pattern in Figure 4(b), the center diffraction spot marked by the white box is still found to be the (206) plane. However, other reflections seen during the transitional stage of the phase transformation cannot be indexed either with cubic or monoclinic symmetry.

Upon further cooling, these metastable reflections disappear and new peaks appear, belonging to the monoclinic symmetry of martensite and indicating that the phase transformation has completed.

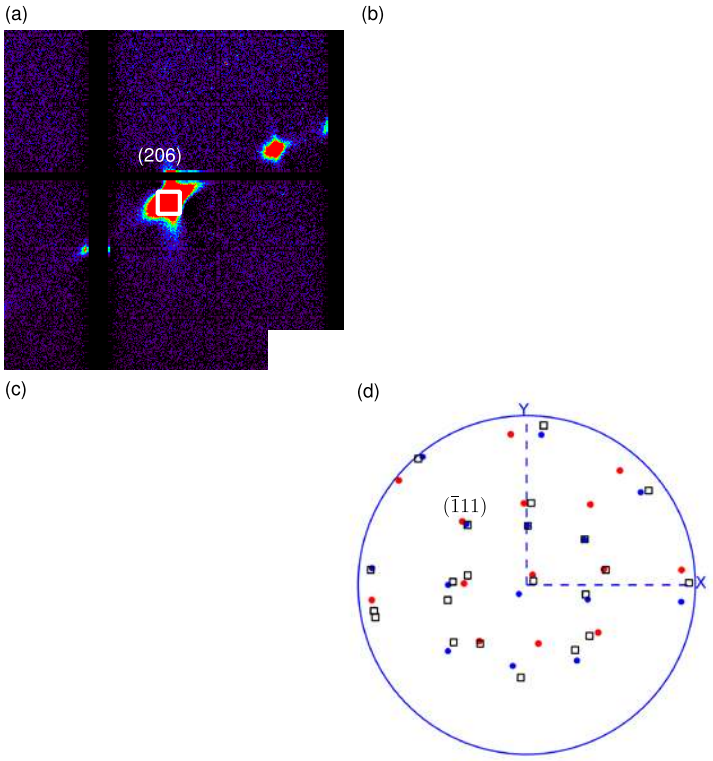

Figure 4. Change of Laue patterns of $Zn_{45}Zu_{30}Cu_{25}$ from (a) pure austenite phase (cubic, Fm-3m) at -10°C, through (b) transition phase to (c) pure martensite phase (monoclinic, P21) at -50°C . Stereographic projections of crystallographic planes of the pure austenite phase (red dots), the transition phase (blue dots) and the martensite planes (black boxes).

The change of lattice orientations during phase transformation reveals the average movement of atoms from one crystal structure to the other, i.e. the transformation pathway. Figure 4(d) shows the stereographic projections of the reciprocal lattices of austenite (red dots), transitional phase (blue dots) and martensite (black boxes) with respect to the rolling (X), transverse (Y) and normal directions (Z) of the sample stage. The sets of red and blue dots in Figure 4(d) are related by a rotation about the axis $(\bar{1}11)$ that maps the reciprocal lattice vectors from austenite to the transitional phase. Due to the structural change, the set of reciprocal lattice vectors of martensite, i.e. the black boxes in Figure 4(d), displays a combination of stretch and rotation deformation from the cubic structured austenite. For a martensitic phase transformation, the set of austenite lattice

vectors is assumed to be deformed into the primitive lattice vectors of martensite by a macroscopic deformation gradient $\boldsymbol{F}$ such that

$$F\,\boldsymbol{E}_A\boldsymbol{L} = \boldsymbol{E}_M, \quad (1)$$

where $\boldsymbol{E}_A$and $\boldsymbol{E}_M$ are the primitive lattice vectors of austenite and martensite respectively and $\boldsymbol{L}$ the *lattice correspondence matrix*. $\boldsymbol{E}_A$ and $\boldsymbol{E}_M$ are directly measured by X-ray Laue microdiffraction, while two solutions for $\boldsymbol{L}$ can be computed, from which two possible orientation relationships between austenite and martensite is derived:

$(2,0,6)_{\mathrm{a}}||\,(2,0,9)_{\mathrm{m}}$ or $(2,0,11)_{\mathrm{m}}$
$(0,0,1)_{\mathrm{a}}||\,(1,0,9)_{\mathrm{m}}$ or $(1,0,10)_{\mathrm{m}}$
$(1,1,9)_{\mathrm{a}}||\,(5,1,36)_{\mathrm{m}}$ or $(5,1,41)_{\mathrm{m}}$
$(2,1,5)_{\mathrm{a}}||\,(7,2,27)_{\mathrm{m}}$ or $(7,2,34)_{\mathrm{m}}$.

3.2. Application of Laue X-ray Microdiffraction in Microelectronic Materials

In the field of microelectronics, new materials and the corresponding design and processes are constantly being developed for improved chip performance. With its unique capabilities, white beam Laue X-ray microdiffraction has proven to be a powerful tool to investigate a wide range of microelectronics-related materials and structures *in-situ* and *in-operando*.

One of the early applications of Laue x-ray microdiffraction for microelectronics was in the electromigration (EM) of metal interconnect lines 56. Electromigration (EM) is a diffusion-controlled mass transport phenomenon driven by the momentum transfer between moving electrons and metal ions, and is a major reliability problem for integrated circuits, as the resulting voids can cause the circuit to fail 57. In both Al and Cu interconnect lines, Laue x-ray microdiffraction observed that EM-induced plastic deformation in the metal lines was manifested as the streaking, broadening, and splitting of the Laue reflections 14 58 59 60 61. It was also found that the occurrence of plastic deformation was correlated to the availability of the ⟨112⟩ crystal directions in the direction of electron flow along the interconnect lines. In this case, the aligned dislocation cores provide an additional diffusion path further degrading EM performance 61. Laue microdiffraction has also been applied to study the response of Sn-based Pb-free solders under EM testing. β-Sn has a body-centered tetragonal crystal structure (a=b=5.84Å, c=3.19Å) and is highly anisotropic. Under EM testing, Sn grains rotated to re-align the a-axis with the direction of the electron flow and lower the effective resistance 62. However, unlike interconnect lines, little to no

plastic deformation was detected in the solder joints. Instead, a build-up of compressive hydrostatic stress was observed at the anode end 63.

More recently, Laue microdiffraction has been used to investigate the materials and structures in three-dimensional integrated circuit (3DIC). 3DIC utilizes vertical integration of two or more dies to overcome the basic material and processing challenges in Moore's Law scaling 64. In a typical 3DIC, Cu through-silicon vias (TSV) are used in conjunction with Cu-Sn microbumps to form the vertical connection between stacked dies 64. For a TSV structure, the mismatch of coefficient of thermal expansion (CTE) between Cu and Si generates considerable amounts of thermal stress in and around the Cu TSV, causing serious thermo-mechanical reliability issues 65. In one study, a set of TSVs was annealed at 200ºC for 1 hour, and Laue microdiffraction was carried out during and after annealing. The thermal stress in Cu, plotted in Figure 5a, shows a strong temperature dependence, which could be related to the microstructure evolution of Cu 66. Further studies observed local plasticity near the top of the Cu vias after thermal cycling, which can be correlated to the height of via extrusion, and thus provided experimental evidence to verify the underlying plastic deformation mechanism of via extrusion (Figure 5b) 67. In Si, stress-induced lattice rotation was observed near the wafer surface and surrounding the TSV 68. This near-surface stress directly affects the mobility of the transistors, requiring defining a device keep-away zone around the TSV 65. To quantitatively interpret the stress in Si, a modeling approach was developed which took into consideration the penetration depth of the high-energy x-ray radiation 69. For TSVs of different diameters, the stress was found to decrease with reduced via diameters 70. Laue x-ray microdiffraction also verified that a thick polymeric liner could act as a stress buffer to reduce stress and the driving force of interfacial delamination compared to a conventional SiO_2 dielectric liner 70.

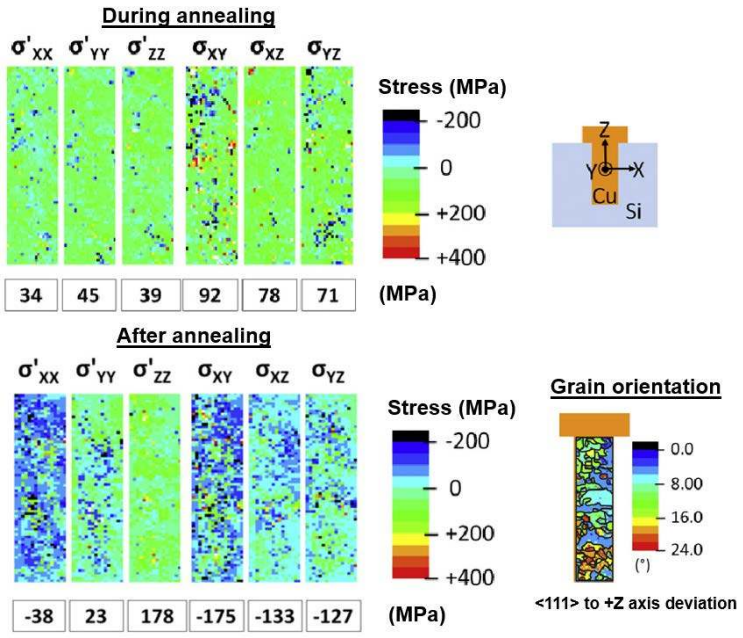

(a)

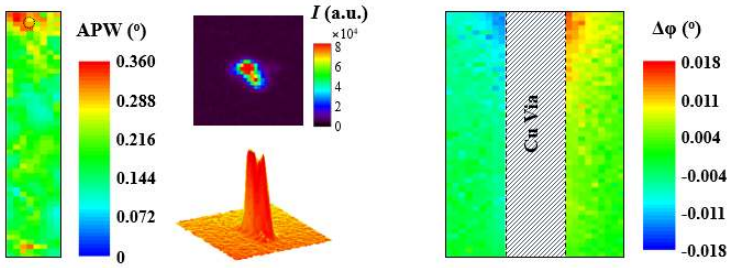

(b)

Figure 5. (a) Deviatoric stress mapping of TSVs during (top) and after (bottom) annealing at 200°C for 1h, and grain orientation mapping after annealing (adapted from 66). (b) Left: Left: Average Peak Width (APW) map for a Cu via shows local plasticity near the top of the TSV, with the broadening of a Cu 024 Laue diffraction shown. Right: Out-of-plane orientation (Δ φ) map for Si surrounding the via indicates lattice bending around the TSV (adapted from reference 65)

4. Current and future developments.

With the development of fast area detectors, it is now possible to scan large portions of a sample in a reasonable amount of time. To take an example, the MAR133 CCD detector, which was in service on BL12.3.2 until 2008 had a readout time of approximately 5 s, so it took about 4 hours to collect a 50x50 μm^2 area of the sample using a 1 μm step size (2500 points) and a 1 s exposure. Today, with the Pilatus 1M hybrid pixel detector, which has virtually no readout time, it takes only

45 minutes to scan the same area. As detector technology progresses towards smaller pixels and higher efficiency and x-ray sources become brighter, data collection time will decrease even further. Scans of large portions of a sample result in a "big data" problem, shifting the bottleneck from data collection to data processing. Laue microdiffraction facilities increasingly rely on the availability of large data storage and high computational speed. The ALS, for instance, is collaborating with the National Energy Research Scientific Computing Center (NERSC) for real-time processing of Laue diffraction data on multicore machines 71.

The combination of fast data collection and speedy data analysis drives the transition from a scanning x-ray microdiffraction mapping tool, toward a real time quantitative imaging technique for texture, strain and defect density. Figure 6 gives an example of data acquired on beamline 12.3.2 and showing the transition of a laser assisted 3D printed part of a nickel-based superalloy, from epitaxial grains growing as columnar dendrites to a "stray" grains polycrystalline region 72 73. The 20,000 Laue patterns collected on that sample were analyzed on a 48 nodes Linux cluster in just a couple of hours

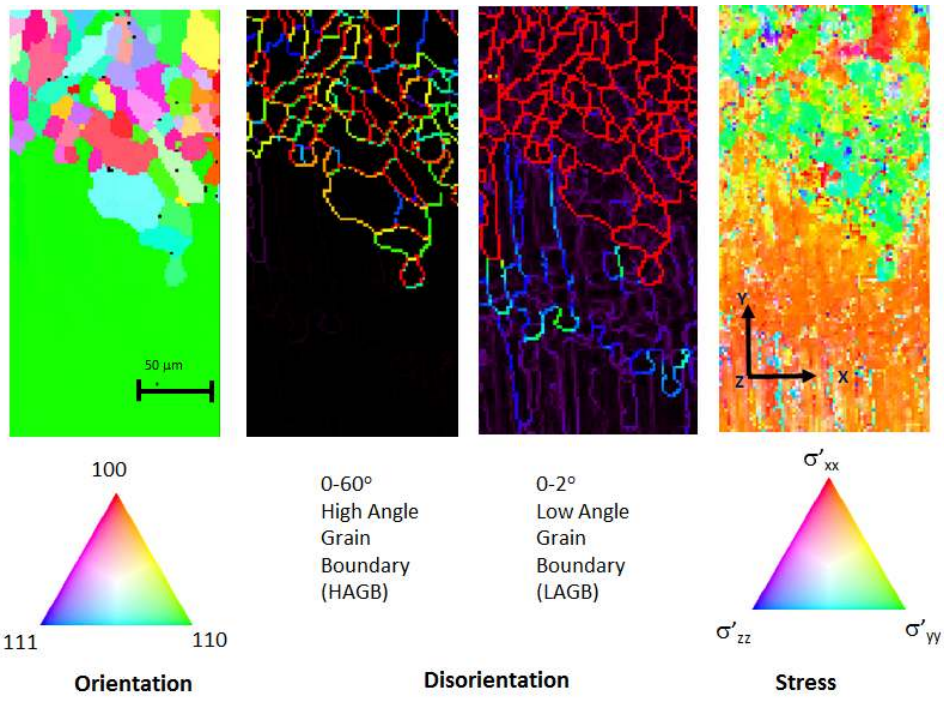

Figure 6. Laue microdiffraction maps of a laser assisted 3D printed Ni-based superalloy showing the transition from a columnar dendritic region to a polycrystalline region. From left to right, crystal orientation, high angle grain boundaries, low angle grain boundaries and deviatoric diagonal stress component maps (adapted from 72)

Two other emerging areas, derived from the technique of x-ray Laue microdiffraction, are structure solution of inorganic compounds with pink beam and serial crystallography with a few percent energy bandpass at Free Electron Laser (FEL) facilities, both taking advantages of fast data collection, offered by a non-monochromatic x-ray beam.

4.1. Structure solution of inorganic compounds with Laue microdiffraction

As new materials become increasingly sophisticated and complex, their structural characterization becomes more difficult. For example, crystals may not be of sufficient quality for conventional single-crystal data collection. They may be embedded in a heterogeneous matrix, or in a constrained environment (e.g. a high-pressure cell). Whatever the material, structural analysis remains central to its characterization and the understanding of its properties. Laue diffraction experiment is an attractive alternative to the conventional monochromatic single-crystal structure analysis, because it not only takes fully advantage of the synchrotron X-ray energy spectrum, but also requires no controlled rotation of the crystal in the very small X-ray beam. By using a broad-bandpass X-ray source, a large number of reflections can be recorded simultaneously in a single exposure (Figure 7(a)). However, determining the structure factors from the reflection measured intensities, as is required for structure analysis, is not straightforward. In order to properly interpret the intensities, various issues such as the deconvolution of harmonics, the correction for energy-dependent factors (absorption, Lorentz coefficient) and the precise determination of the effective incident spectrum have to be addressed. For small molecule and inorganic samples, the use of pre-corrected Lorentz and polarization factors, combined with the "reverse method" based on the use of a single Laue pattern of a well-known crystal has been devised (Figure 7(b)) 74.

Using the methodology described above, the crystal structure of an indigo/silicalite organic/inorganic hybrid, an analog of ancient Maya Blue, has been determined by combining Laue microdiffraction with powder diffraction 75. In particular, Laue microdiffraction was used to map the indigo distribution within a single crystal. By following the Laue intensity evolution of relevant reflections, both empty monoclinic domains and indigo-induced orthorhombic domains were identified. The Laue diffraction data further indicated that the most probable space group of the orthorhombic domains was Pnma rather than $P2_12_12_1$ (Figure 7c). Structure solution and

refinement using Laue microdiffraction data were also carried out for three model samples (sanidine, potassium titanyl phosphate (KTP), and ZSM-5 zeolite), using a serial snapshot crystallography approach 76. This shows that Laue microdiffraction can be a good alternative to solve and refine the structure of micron-to-submicron crystals when classic crystallography methods cannot be used.

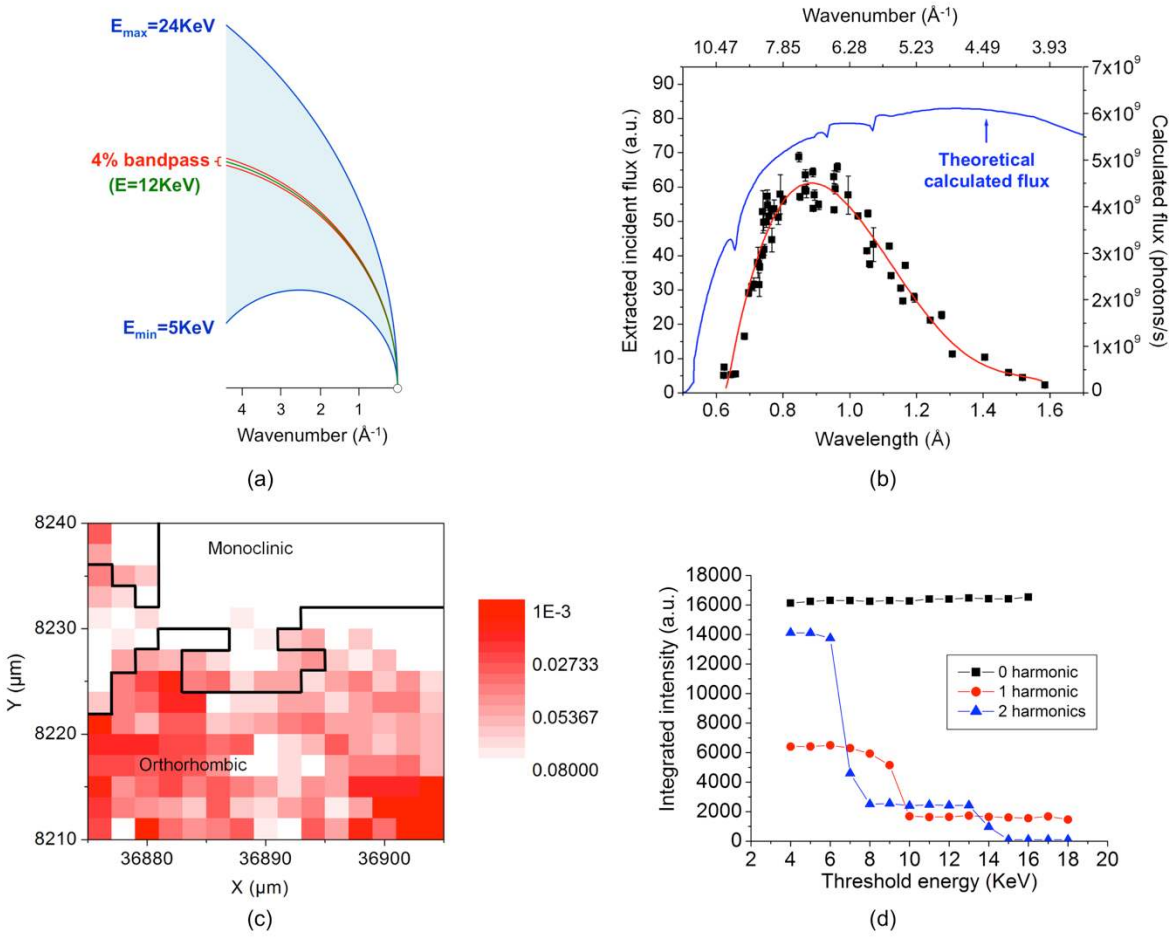

Figure 7. a) Ewald construction for Laue mode (5-24keV), monochromatic mode (12keV), and 4% bandpass mode (average energy 12keV). Accessible reflections fall into the shaded areas; b) Incident flux curve (convoluted with the detector response), determined from a single Laue pattern of calcite. The theoretical calculated incident white beam flux is also displayed for comparison; c) Distribution of the I(4 1 -6)/I(8 1 -9) ratio over an indigo-doped silicalite single crystal. The increase in the intensity ratio from orthorhombic to monoclinic domain is consistent with the space group *Pnma*;

4.2. Laue microdiffraction and Free Electron Laser

With the development of X-ray free-electron laser (X-FEL) sources that create ultra-short X-ray pulses of unprecedented brilliance, a new option for the structural characterization of microcrystalline inorganic materials is arising 77. Any crystal placed in an X-FEL beam will be destroyed, but not before one diffraction pattern is collected. To get a full data set, therefore, many randomly oriented stationary crystals have to be measured. To date, most activity in the realm of structure analysis using a Serial Femtosecond Crystallography (SFC) approach with X-FEL radiation has focused on macromolecular systems 78.

The SwissFEL facility 79, scheduled to be operational in 2017, will have a unique feature: the bandpass of the X-ray beam will be adjustable to give as much as a 4% energy spread, an intermediate mode between monochromatic and white beam (Laue) diffraction (Figure 7(a)). To evaluate the possibility of exploiting this option for microcrystal diffraction of crystals with relatively small unit cells (≤ 25000 Å^3), data for typical inorganic structures were simulated 80. It was found that with the 4%-energy-bandpass mode, not only more reflections can be recorded per shot, but the intensities can also be measured more reliably. New indexing algorithms 81 also showed that individual patterns of up to 10 crystals, measured simultaneously, could be indexed, and that intensities could be extracted reliably for structure analysis. This means that even with a single shot, at least a partial analysis of the crystal structure is possible, and this offers tantalizing possibilities for time-resolved studies.

8. Conclusion

Synchrotron white beam Laue x-ray microdiffraction used in scanning mode has greatly matured as a technique over the last decade. With the ever increasing brightness achievable at modern synchrotron facilities, progress in x-ray focusing optics and fast 2D detector technology, as well as the use of parallel computing for near real time data reduction, Laue x-ray microdiffraction is transitioning from a microstructure mapping tool into a quantitative microstructural imaging tool. Information such as phase, grain orientation, strain and defect density distribution can be readily obtained from the analysis of thousands of Laue patterns. The technique as is known today has a wide range of applications beyond the study of the mechanical properties of thin film materials

used in electronic devices. Recent developments include the measurements of stress in geological samples 82, the mapping of phases and stresses in ancient artifacts 83, orientation imaging in functional materials 84 and biominerals 85 . As new micro- and nanodiffraction facilities with white beam capabilities are being constructed around the world, it is likely that the use of scanning Laue x-ray microdiffraction imaging will become widespread across several disciplines. For the interested readers, the technique is described in several chapters of the recently published book *Strain and Dislocation Gradients from Diffraction: Spatially-Resolved Local Structure and Defects* by R. Barabash and G.E. Ice 86 .

Acknowledgements: The Advanced Light Source is supported by the Director, Office of Science, Office of Basic Energy Sciences, of the U.S. Department of Energy under Contract No. DE-AC02-05CH11231.

Bibliography

1. W. Friedrich, P. Knipping & M. V. Laue, *Sitzungs-Berichte der Königlich-Bayerischen Akademie der Wissenschaften, Mathematisch-Physikalische Klasse* **42**, 303 (1912).
2. W. L. Bragg, *Proceedings of the Cambridge Philosophical Society* **17**, 43 (1913).
3. M. M. Woolfson, *An introduction to X-ray crystallography* (Cambridge University Press, 1997).
4. R. E. Dinnebier & S. L. J. Billinge eds., *Powder diffraction: theory and practice* (2008).
5. D. K. Bowen & B. K. Tanner, *High resolution X-ray diffractometry and topograhy* (CRC press, 2005).
6. K. Moffat, D. Szebenyi & D. Bilderback, *Science*, 1423 (1984).
7. J. R. Helliwell, J. Habash, D. W. J. Cruikshank *et al.*, *Journal of Applied Crystallography* **22** (5), 483 (1989).
8. K. Moffat & J. R. Helliwel, in *Synchrotron Radiation in Chemistry and Biology III*, p. 61 (1989).
9. D. Bourgeois, B. Vallone, A. Alessandro *et al.*, *Proceedings of the National Academy of Sciences* **100** (15), 8704 (2003).
10. H. R. Wenk, F. Heidelbach, D. Chateigner *et al.*, *Journal of Synchrotron Radiation* **4** (2), 95 (1997).
11. J. Chung & G. Ice, *Journal of Applied Physics* **86** (9), 5249 (1999).
12. O. Tschauner, P. D. Asimow, N. Kostandova *et al.*, *Proceedings of the National Academy of Sciences* **106** (33), 13691 (2009).
13. A. Mehta, E. J. Nelson, S. M. Webb *et al.*, *Advanced Materials* **19** (9), 1183 (2007).

14. B. C. Valek, J. C. Bravman, N. Tamura *et al.*, *Applied Physics Letters* **81**, 4168 (2002).
15. J. J. Bozzola & L. D. Russell, *Electron microscopy: principles and techniques for biologists* (Jones & Bartlett Learning, 1999).
16. O. E. Myers Jr, *American Journal of Physics* **19** (6), 359 (1951).
17. B. Lai, W. Yun, D. G. Legnini *et al.*, *Applied Physics Letters* **61** (16), 1877 (1992).
18. Y. S. Chu, J. M. Yi, F. De Carlo *et al.*, *Applied Physics Letters* **92** (10), 103119 (2008).
19. W. Chao, J. Kim, S. Rekawa *et al.*, *Optics Express* **17** (20), 17669 (2009).
20. A. Snigirev, V. Kohn, I. Snigireva *et al.*, *Nature* **384** (6604), 49 (1996).
21. A. A. Snigirev, I. Snigireva, M. Drakopoulos *et al.*, in *Proc. SPIE 5195, Crystals, Multilayers, and Other Synchrotron Optics*, p. 21 (2003).
22. C. G. Schroer, M. Kuhlmann, U. T. Hunger *et al.*, *Applied Physics Letters* **82** (9), 1485 (2003).
23. P. Kirkpatrick & A. V. Baez, *Journal of the Optical Society of America* **38** (9), 766 (1948).
24. H. Mimura, S. Matsuyama, H. Yumoto *et al.*, *Japanese Journal of Applied Physics* **44** (4L), L539 (2005).
25. W. Liu, G. E. Ice, J. Z. Tischler *et al.*, *Review of Scientific Instruments* **76** (11), 113701 (2005).
26. W. Liu, G. E. Ice, L. Assoufid *et al.*, *Journal of Synchrotron Radiation* **18** (4), 575 (2011).
27. G. E. Ice & B. C. Larson, *Advanced Engineering Materials* **2** (10), 643 (2000).
28. M. Kunz, N. Tamura, K. Chen *et al.*, *Review of Scientific Instruments* **80** (3), 035108 (2009).
29. N. Tamura, R. S. Celestre, A. A. MacDowell *et al.*, *Review of scientific instruments* **73** (3), 1369 (2002).
30. O. Ulrich, X. Biquard, P. Bleuet *et al.*, *Review of Science Instruments* **82** (3), 033908 (2011).
31. J. H. Park, J. Park, K. B. Lee *et al.*, *Applied Physics Letters* **91**, 012906 (2007).
32. R. Feng, A. Gerson & G. Ice, in *AIP Conference Proceedings* , p. 872 (2007), Vol. 879.
33. R. Maaβ, D. Grolimund & S. V. Petegem, *Applied Physics Letters* **89** (15), 151905 (2006).
34. F. Hofmann, X. Song, I. Dolbnya *et al.*, *Procedia Engineering* **1** (1), 193 (2009).
35. N. Tamura, M. Kunz & K. Chen, *Materials Science and Engineering: A* **524** (1), 28 (2009).
36. Y. Sheng, V. Y. Valeriy & K. Goldberg, *X-ray Optics and Instrumentation* **784732**, 1-9 (2010).
37. K. S. Liang, G. H. Luo, J. R. Chen *et al.*, *Synchrotron Radiation News* **22** (5), 13 (2009).
38. A. B. Greninger, *Transactions of the American Institute of Mining and Metallurgical Engineers* **61** (117) (1935).
39. J. S. Chung, N. Tamura, G. E. Ice *et al.*, in *MRS Proceedings*, p. 169 (Cambridge University Press, 1999), Vol. 563.

40. N. Tamura, B. C. Valeck & R. Spolenak, in *MRS Proceedings*, p. 8 (Cambridge University Press, 2000), Vol. 612.
41. R. I. Barabash, G. E. Ice, B. C. Larson *et al.*, *Review of Scientific Instruments* **73** (3), 1652 (2002).
42. B. C. Larson, W. Yang, G. E. Ice *et al.*, *Nature* **415** (6874), 887 (2002).
43. W. Liu & G. E. Ice, in *Strain and Dislocation Gradients from Diffraction*, p. 53 (2014).
44. J. D. Budai, W. Yang, B. C. Larson *et al.*, in *Materials Science Forum*, p. 1373 (2004), Vol. 467.
45. N. B. Morgan, *Materials Science and Engineering: A* **378** (1), 16 (2004).
46. H. E. Karaca, I. Karaman, B. Basaran *et al.*, *Advanced Functional Materials* **19** (7), 983 (2009).
47. V. Srivastava, X. Chen & R. D. James, *Applied Physics Letters* **97**, 014101 (2010).
48. V. Srivastava, Y. Song, K. Bhatti *et al.*, *Advaced Energy Materials* **1** (1), 97 (2011).
49. Y. Song, K. P. Bhatti, V. Srivastava *et al.*, *Energy & Environmental Science* **6** (4), 1315 (2013).
50. Y. Song, *Physical Chemistry Chemical Physics* **16** (25), 12750 (2014).
51. X. Chen, S. Cao, T. Ikeda *et al.*, *Acta Materialia* **59** (15), 6124 (2011).
52. Y. Song, X. Chen, V. Dabada *et al.*, *Nature* **502** (7469), 85-88 (2013).
53. C. Chluba, W. Ge, R. L. d. Miranda *et al.*, *Science* **348** (6238), 1004 (2015).
54. X. Chen, V. Srivastava, V. Dabade *et al.*, *Journal of the Mechanics and Physics of Solids* **61** (12), 2566 (2013).
55. X. Chen, Y. Song, N. Tamura *et al.*, *arXiv preprint arXiv: 1501.05064*.
56. P. C. Wang, G. S. Cargill, I. C. Noyan *et al.*, *Applied Physics Letters* **72**, 1296 (1998).
57. P. S. Ho & T. Kwok, *Reports Prog. Phys.* **52**, 301 (1989).
58. B. C. Valek, N. Tamura, R. Spolenak *et al.*, *Journal of Applied Physices* **94**, 3757 (2003).
59. R. I. Barabash, G. E. Ice, N. Tamura *et al.*, *Journal of Applied Physics* **93**, 5701 (2003).
60. K. Chen, N. Tamura, B. C. Valek *et al.*, *Journal of Applied Physics* **104**, 013513 (2008).
61. A. S. Budiman, P. R. Besser, C. S. Hau-Riege *et al.*, *Journal of Electron. Mater.* **38**, 379 (2009).
62. K. Chen, N. Tamura & K. N. Tu, *MRS Proceedings* **1116**, 1116-I05 (2008).
63. K. Chen, N. Tamura, M. Kunz *et al.*, *Journal of Applied Physics* **106**, 023502 (2009).
64. S. S. Iyer, in *MRS Bulletin*, p. 225 (2015), Vol. 40.
65. T. Jiang, R. H. J. Im & P. S. Ho, in *MRS Bulletin*, p. 248 (2015), Vol. 40.
66. A. S. Budiman, H. A. S. Shin, B. J. Kim *et al.*, *Microelectronics Reliability* **52**, 530 (2012).
67. T. Jiang, C. Wu, L. Spinella *et al.*, *Applied Physics Letters* **103**, 211906 (2013).
68. T. Jiang, C. Wu, N. Tamura *et al.*, *IEEE Trans on, Device and Materials Reliability* **14**, 698 (2014).
69. X. Liu, P. A. Thadesar, C. L. Taylor *et al.*, *Applied Physics Letters* **103**, 022107 (2013).

70. X. Liu, P. A. Thadesar, C. L. Taylor *et al.*, *Journal of Applied Physics* **114**, 064908 (2013).
71. J. Deslippe, A. Essiari, S. J. Patton *et al.*, in *Proceedings of the 9th Workshop on Workflows in Support of Large-Scale Science IEEE Press*, p. 31 (2014).
72. Y. Li, D. Qian, J. Xue *et al.*, *Applied Physics Letters* **107** (18), 181902 (2015).
73. J. Xue, A. Zhang, Y. Li *et al.*, *Scientific Reports* **5** (2015).
74. C. Dejoie, M. Kunz, N. Tamura *et al.*, *Applied Crystallography* **44** (1), 177 (2011).
75. C. Dejoie, P. Martinetto, N. Tamura *et al.*, *The Journal of physical Chemistry C* **118** (48), 28032 (2014).
76. C. Dejoie, L. B. McCusker, C. Baerlocher *et al.*, *Journal of Applied Crystallography* **46** (3), 791 (2013).
77. H. N. Chapman, P. Fromme, A. Barty *et al.*, *Nature* **470** (7332), 73 (2011).
78. I. Schlichting, *IUCrJ* **2** (2), 246 (2015).
79. B. D. Patterson, P. Beaud, H. H. Braun *et al.*, *CHIMIA Internatinal Journal for Chemistry* **68** (1), 73 (2014).
80. C. Dejoie, L. B. McCusker, C. Baerlocher *et al.*, *Journal of Applied Crystallography* **46** (6), 1805 (2013).
81. C. Dejoie, S. Smeets, C. Baerlocher *et al.*, *IUCrJ* **2** (3), 361 (2015).
82. K. Chen, M. Kunz, N. Tamura *et al.*, *Geology* **43** (3), 2015 (2015).
83. C. Dejoie, N. Tamura, M. Kunz *et al.*, *Journal of Applied Crystallography* **48** (5), 1522 (2015).
84. E. Y. Ma, Y. T. Cui, Y. Ueda *et al.*, *Science* **350** (6260), 538 (2015).
85. I. C. Olson, R. A. Metzler, N. Tamura *et al.*, *Journal of Structural Biology* **183** (2), 180 (2013).
86. R. Barabash & G. Ice eds., *Strain and Dislocation Gradients from Diffraction: Spatially-Resolved Local Structure and Defects* (World Scientific, 2014).